https://doi.org/10.1016/j.intermet.2019.106553

Tuning deformation behavior of $Cu_{0.5}CoNiCrAl$ high-entropy alloy via cooling rate gradient: An atomistic study

Shidong Feng [a,b], Lin Li [c], K.C. Chan [a,*], Lei Zhao [a], Shaopeng Pan [d], Limin Wang [b,*], Riping Liu [b]

[a] *Advanced Manufacturing Technology Research Centre, Department of Industrial and Systems Engineering, The Hong Kong Polytechnic University, 999077, Hong Kong.*

[b] *State Key Laboratory of Metastable Materials Science and Technology, Yanshan University, Qinhuangdao 066004, China*

[c] *Department of Metallurgical and Materials Engineering, The University of Alabama, Tuscaloosa, AL 35487, USA*

[d] *College of Materials Science and Engineering, Taiyuan University of Technology, Taiyuan, 030024, China*

Submitted to

Intermetallics

As a full paper

* Corresponding author.

E-mail address: kc.chan@polyu.edu.hk (K.C. Chan);

limin_wang@ysu.edu.cn (Limin Wang).

Abstract

The deformation behaviors of body-centered cubic $Cu_{0.5}CoNiCrAl$ high-entropy alloys processed by the cooling rate gradient are investigated by the molecular dynamics simulations. The plastic deformation ability of the high-entropy alloy is significantly improved by triggering multiple-type dislocation slips along different deformation paths. The cooling rate gradient introduces abundant atomic vacancies, proliferating the nucleation sites of dislocations. Additionally, the nucleation barriers of dislocations are reduced by the resultant structural disorder, high potential energy and chemical segregation. Consequently, the cooling rate gradient enhances the structural heterogeneity, promoting the formation of multiple deformation paths and preventing strain localization.

Keywords: A. high–entropy alloys; B. dislocation structure; D. microstructure; D. grain boundary; D. plastic deformation unit; E. molecular dynamic simulation

1. Introduction

High-entropy alloys (HEAs) containing several principle elements with equal or nearly equal atomic ratios have been widely developed [1-3]. It is postulated that high configurational entropy promotes the formation of simple disordered solid solutions, such as face-centered cubic (FCC), body-centered cubic (BCC) and hexagonal close-packed (HCP) [4-7]. Consequently, HEAs possess excellent thermal and mechanical properties, such as high strength, high hardness, high temperature stability, high corrosion resistance and excellent soft magnetic properties [8-12]. The fundamental deformation mechanisms in conventional crystal alloys, including dislocation slip, grain boundary sliding and twinning, have all been observed in HEAs [13-16]; and yet the details are argue to be different due to the distortion of the lattice structures in HEAs. The deformation behaviors of FCC and HCP HEAs have attracted considerable

investigation [17, 18]. For example, by regulating the microstructure, an FCC high-entropy alloy with ordered nano-precipitation strengthening is developed, which greatly improves the strength and high-temperature mechanical properties without significantly reducing the plasticity [19]. Ding et al. found that the energy difference between the FCC and HCP phases strongly correlates with the local ordering, affecting the transformation-induced plasticity [20]. Through *in-situ* neutron diffraction analysis, the work hardening behavior of plasticity in HEAs are revealed via FCC-to-HCP transformations, providing a mechanistic understanding of the superior strength and ductility [21]. However, the study on deformation behaviors of BCC HEAs is quite limited, partly due to the fact that most BCC HEAs are strong and yet brittle, can fail via strain localization by forming shear bands [22, 23].

In this work, we study the deformation behaviors of a BCC $Cu_{0.5}$CoNiCrAl HEA using molecular dynamics (MD) simulations. By utilizing the cooling rate gradient, a significantly enhanced plasticity is observed in the solidified HEA sample. The structural heterogeneity is able to trigger multiple-type dislocation slips along different deformation paths, preventing strain localization. A detailed atomistic study is provided, revealing the structural disorder and high potential energy proliferate the dislocation nucleation sites as well as lower the nucleation barriers. We envision our discovery can potentially guide the fabrication of plastically enhanced BCC HEAs via *in-situ* tuning the processing parameters.

2. Methodology

In describing the interaction between the elements of Cu–Co–Ni-Cr-Al, the embedded atom method (EAM) potential developed by Zhou was adopted [24], which modifies the alloy EAM potential database that enables alloy potentials from 17 metals (Cu, Co, Ni, Cr, Al, Ag, Au, Pd, Pt, Pb, Fe, Mo, Ta, W, Mg, Ti and Zr) to be created

from normalized elemental potentials [25, 26]. The alloy EAM potential has been successfully used to simulate metal multilayer systems [26-28], BCC $Co_{16.67}Fe_{36.67}Ni_{16.67}Ti_{30}$ and AlCoCrCuFeNi HEAs [29-31]. To validate the potential, the relationship between the cohesive energy and lattice constant of the BCC $Cu_{0.5}$CoNiCrAl HEA was investigated, as shown in Fig. 1. The minimum value of the cohesive energy -3.5243 eV corresponds to the equilibrium lattice constant of 3.2261 Å at 300 K. The estimated BCC lattice parameter is in reasonably agreement with experiment (2.892 Å) [32], although there is a slight overestimation. The followings are the reasons for such discrepancy. In Yeh'work, the lattice constant of the deposited BCC $Cu_{0.5}$CoNiCrAl polycrystalline thin film is determined from the XRD peaks. Because nanosized crystallites and an amorphous phase are formed as the amorphous inter crystal boundaries, the XRD peaks are largely broadened and superposed on a broad peak, with a base of over 10 deg. Meanwhile, the composition of the sputtered $Cu_{0.5}$CoNiCrAl thin films is characterized by EDS as Cu: 11 pct, Co: 20 pct, Ni: 22 pct, Cr: 21 pct, and Al: 26 pct in element fraction, which is different from that in our model BCC $Cu_{0.5}$CoNiCrAl HEA. Random occupation of variously sized atoms on lattice points causes the crystalline lattices to be severely distorted. They all contribute to the discrepancy of the predicted and experimental lattice constants. The lattice constant has been used to estimate the bulk modulus (163.2 GPa) of the BCC $Cu_{0.5}$CoNiCrAl HEA. Although it is not able to directly compare with the experimental results as there is no experimental bulk modulus available in the literature, the estimated bulk modulus is within the range (156.5 ~ 219.3 GPa) of the experimental bulk modulus of the Al_xCoCrCuFeNi HEAs reported in the literatures [33].

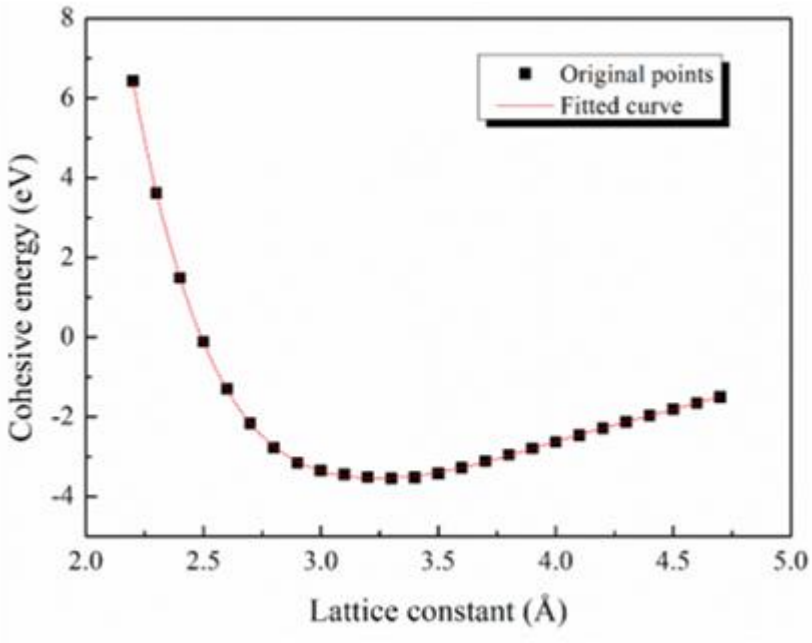

Fig. 1 The cohesive energy-lattice constant curve of the BCC $Cu_{0.5}CoNiCrAl$ HEA.

Though the DFT calculation can describe the bonding properties and binding energy [34, 35], it is limited by the small number of atoms. The MD simulation using LAMMPS was adopted [36], and an *NPT* ensemble with a Nosé-Hoover thermostat and Parrinel-Rahmann barostat was applied [37, 38]. The initial model of $Cu_{0.5}CoNiCrAl$, including 80,000 random atoms ($21 \times 5.2 \times 10.5$ nm^3), was first equilibrated for 1 ns at 3000 K (above the melting temperature) and hydrostatic pressure 0 GPa under periodic boundary conditions (PBCs). Then it was quenched to 300 K under hydrostatic pressure 60 GPa at different cooling rates 10^{11} K/s, 5 x 10^{11} K/s and 10^{12} K/s, respectively. To ensure the alloy with a single crystalline phase, the hydrostatic pressure 60 GPa was applied during the quenching process. After repeated testing, it is found that the fraction of the single crystalline (BCC) phase is high (~95%) when the hydrostatic pressure is 60 GPa. And when the hydrostatic pressure is less than 60 GPa, a polycrystalline structure with different crystalline phases is obtained. Fig. 2 shows the schematic diagram of fabrication of the HEA and the HEA-L nanolaminates. The HEA-L

nanolaminate (including 320,000 atoms) was fabricated by HEAs prepared at different cooling rates (i.e., 10^{12} K/s, 10^{11} K/s, 5 x 10^{11} K/s and 10^{12} K/s), while the HEA nanolaminate (including 320,000 atoms) was made up of HEAs prepared at the same cooling rate 1 x 10^{12} K/s. In order to avoid the accumulation gap between the layers, the HEA and HEA-L nanolaminates were relaxed for 1.5 ns at hydrostatic pressure 1.5 GPa and 300 K under PBCs. To release the excess energy, they were relaxed subsequently for 1.5 ns at hydrostatic pressure 0 GPa and 300 K under PBCs.

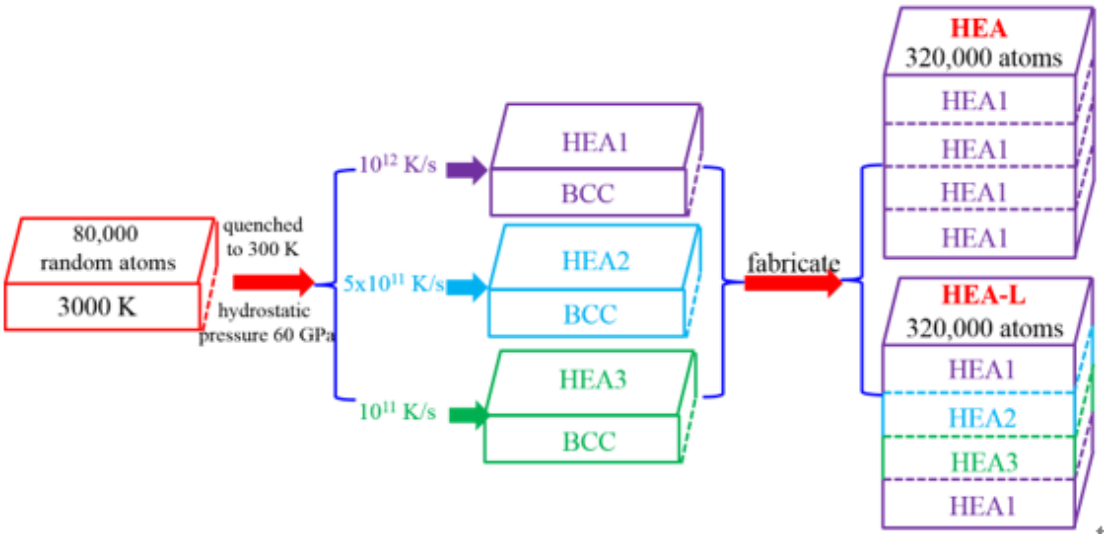

Fig. 2 The schematic diagram of fabrication of HEA and the HEA-L nanolaminates.

To confirm the random chemical distribution, pair correlation functions (PDF) for each element and the distribution of elements in the $Cu_{0.5}$CoNiCrAl HEA at 300K with a cooling rate of 10^{12} K/s are computed and displayed in Fig. 3. They prove the uniform chemical distribution in the $Cu_{0.5}$CoNiCrAl HEA. The PDF for each element in the $Cu_{0.5}$CoNiCrAl HEA with cooling rates of 10^{11} K/s and 5 x 10^{11} K/s are similar to that in the $Cu_{0.5}$CoNiCrAl HEA with the cooling rate of 10^{12} K/s, so they are not shown. Fig. 4 shows the total PDF of HEAs prepared at different cooling rates. It is seen that the structures of HEAs prepared at the three cooling rates all consist of crystallites, as evinced by multiple peaks of the PDFs.

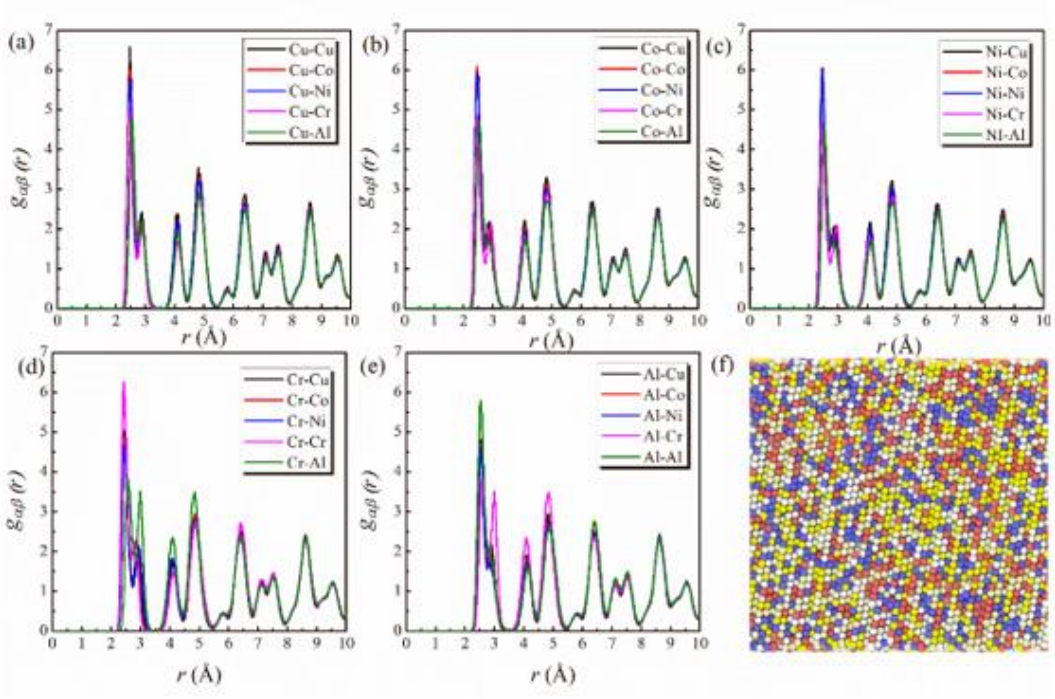

Fig. 3 (a)-(e) Pair distribution functions and (f) element distribution of the $Cu_{0.5}CoNiCrAl$ HEA with a cooling rate of 10^{12} K/s. Different colors represent different elements: Cu in purple, Co in blue, Ni in pale yellow, Cr in white, and Al in yellow.

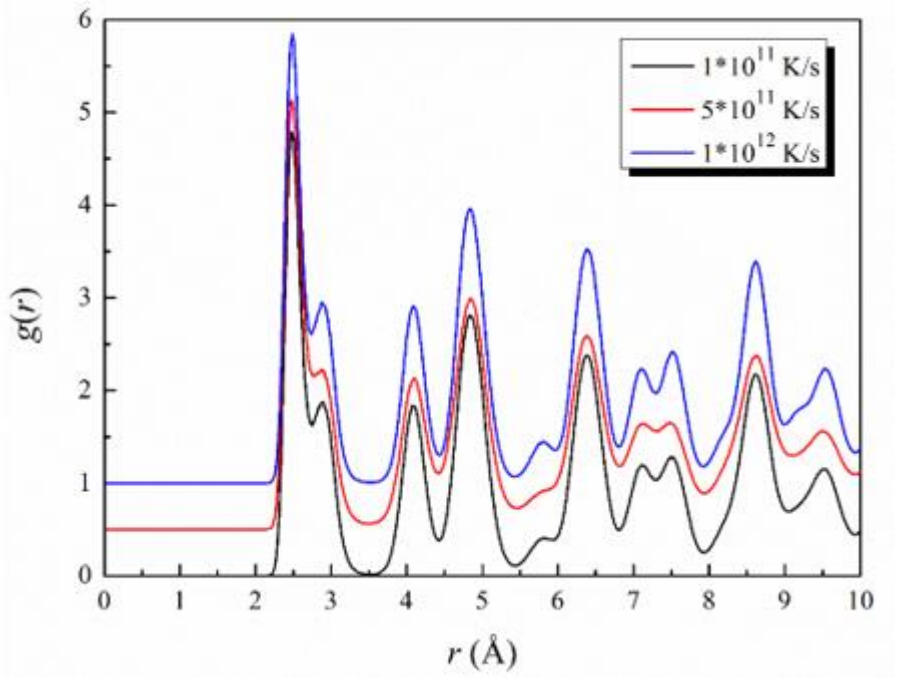

Fig. 4 Pair distribution functions of HEAs prepared with different cooling rates.

The uniaxial compressive strain along the Z-direction was imposed. During the compression process, the HEAs were simulated by moving the rigid atoms at one end along the Z-direction, while keeping the rigid atoms at the other end fixed. In each action, the moving end was displaced by 0.016 nm at an instance of time, followed by the relaxation of the whole sample for 10 ps. The system is relaxed every step upon an instantaneous strain, allowing the system to sufficiently evolve to accommodate further deformation. A typical strain rate is 4×10^7 s^{-1} along the Z-direction at the temperature of 300 K. The PBCs were in the Y- and Z-directions, while the X-direction was the free surface to allow shear offset (inhomgenous deformation) on the free surface [39]. The open tool (OVITO) was used for visualization [40].

3. Results and discussion

3.1. Lattice orientation

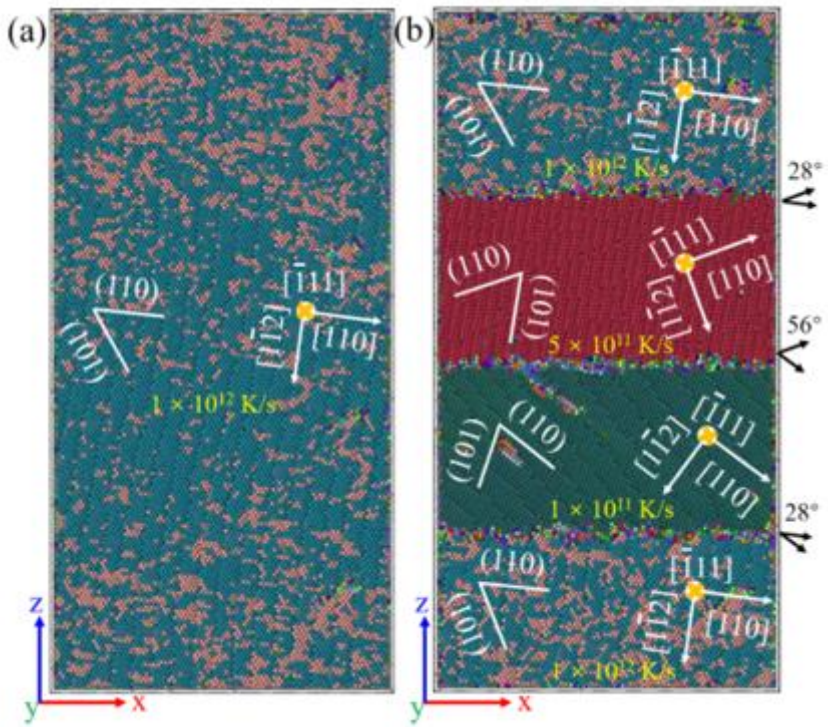

Fig. 5 The model schematic showing the crystal orientations of (a) the HEA and (b) the HEA-L. Different local lattice orientations are colored by the PTM function.

The polyhedral template matching (PTM) function of OVITO can be used to compute the local lattice orientation for each atom in a (poly)crystal [41]. The HEA-L in Fig. 5 made up of grains with different orientations is characterized by the crystal orientation index. The grain orientation [$\bar{1}11$] along the y axis is the same, while the grain orientations [110] and [$1\bar{1}2$] are different for the HEAs prepared at different cooling rates. In detail, the cooling rate is used to control the temperature gradient, influencing the orientation growth of the grains in the HEA-L. It's worth noting that if analysis models have enough space, various kinds of crystal orientation could appear during the cooling process. The hydrostatic pressure of 60 GPa can limit the space so we can obtain the HEA models with the same <111> direction along the y direction even though at different cooling rates.

3.2. Stress-strain curve and atomic local shear strain

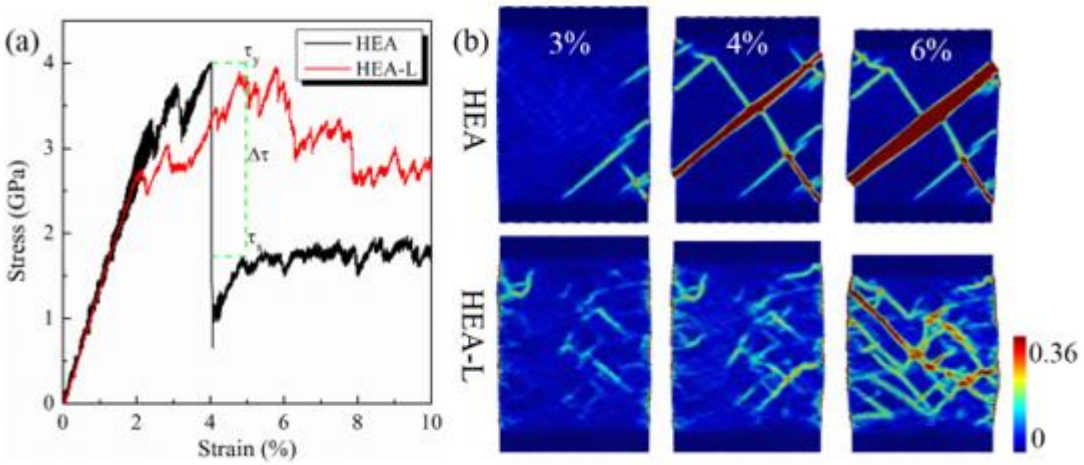

Fig. 6 (a) The compressive stress-strain curves and (b) snapshots of local atomic shear strain η_i^{Mises} of the HEA and the HEA-L at strains of 3%, 4%, and 6%.

The compressive stress-strain curves of the HEA and the HEA-L are shown in Fig. 6a. For the HEA-L with the cooling rate gradient, the decrease in stress after reaching the maximum stress τ_y is gradual, while the HEA without the cooling rate gradient

experiences a sudden drop after reaching the maximum stress τ_y, corresponding to unstable deformation. After the stress drop, the stress-strain curve of the HEA reaches the flow stress τ_s. The difference between the maximum stress τ_y and the flow stress τ_s can reflect the degree of deformation localization. The larger the $\Delta\tau$, the more localized the deformation. Compared to the HEA, the stress drop $\Delta\tau$ of the HEA-L decreases significantly, showing the enhancement in stable deformation ability. To understand the significant difference in the stress drop, the local atomic shear strain η_i^{Mises} of the HEA and the HEA-L at strains of 3%, 4%, and 6% are shown in Fig. 6b. η_i^{Mises} measures the degree of local deformation, according to the difference in atomic displacement between the current state and the reference state [42]. In this work, we take the undeformed state as the reference state. As shown in Fig. 6b, corresponding to the abrupt stress drop upon yielding in the HEA, a highly localized strain path is developed in the form of a dominant shear band throughout the HEA sample. Further plastic flow is mediated by strain localization via shear band thickening. On the other hand, for the HEA-L in Fig. 6b, homogenous deformation is achieved via developing multiple strain paths. Further straining, these strain paths gradually intersect and overlap, propagating in multiple directions and preventing localized flow. This enhanced deformability is attributed to grain boundaries of the HEA-L, which are closely related to the different lattice orientations obtained from the PTM function in the HEA-L. Compared to the HEA, the different lattice orientations in the HEA-L induced by the cooling rate gradient can trigger the formation of multiple grain boundaries, enhancing structural heterogeneity and promoting the formation of multiple deformation paths. Although the composition in the HEA and HEA-L is the same, the deformation ability of the HEA-L with the cooling rate gradient is effectively enhanced by the formation of multiple strain paths.

3.3. Dislocation

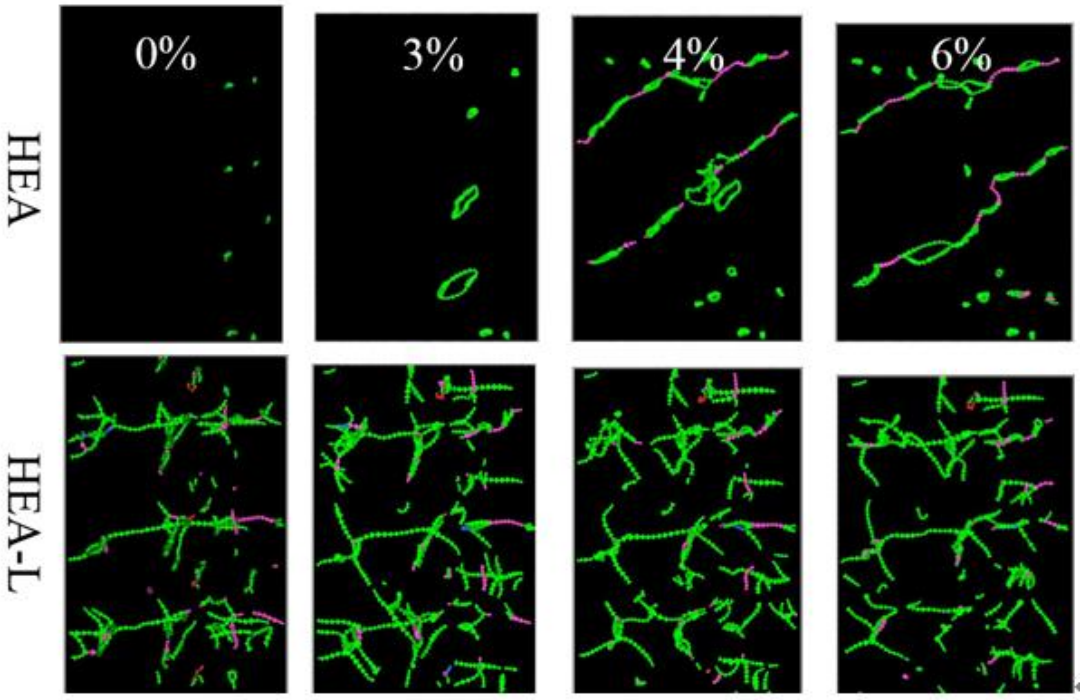

Fig. 7 The distribution of dislocations in the HEA and the HEA-L at strains of 0%, 3%, 4% and 6%. Different colors represent different dislocation type: 1/2<111> in green, <100> in pink, <110> in blue and other in red.

The formation of multiple strains is related to the activity of the flow defect dislocations in the HEA samples. The dislocation extraction algorithm (DXA) [43] is employed to identify all dislocations and the Burgers vectors in a crystal, outputting line representation of the dislocation defects. Fig. 7 shows the distribution of dislocations at strains of 0%, 3%, 4%, and 6% in the HEA and the HEA-L, respectively. For the HEA, nearly no dislocation is observed at the strain of 0%. And a few dislocation loops with Burges vector 1/2<111> are formed at a strain of 3%, corresponding to some small local strains in Fig. 6b. Two parallel 45° dislocation lines are developed throughout the HEA at the strain of 4%, whereas the abrupt stress drop is noted after reaching the maximum stress (ref. to Fig. 6a). At a strain of 6%, the

spacing between the two parallel dislocation lines increases with a slight increase in dislocation density. Correspondingly, a highly localized shear band is developed (ref. to Fig. 6b). On the other hand, for the HEA-L, at the strain of 0%, many misfit dislocations are formed to accommodate the grain boundaries induced by the cooling rate gradient. And a large number of dislocation lines in different directions are observed, carrying the plastic flow of HEA-L from the strain of 3% to 6%, avoiding the formation of a single dislocation path.

Fig. 8 shows the evolution of the dislocation density (total length of dislocation line divided by the volume) as a function of the macroscopic strain. The density of the total dislocations, the main dislocation 1/2<111> and other dislocations are shown, respectively. Overall, the dislocation density of the HEA-L is significantly higher than that of the HEA, suggesting that multiple dislocations form in the HEA-L to accommodate the orientation variation of the HEA-L induced by the cooling rate gradient. In Fig. 8, the trend of the density change of total dislocations is consistent with that of the main dislocation 1/2<111>. For the HEA, the density of total dislocations, the main dislocation 1/2<111> and other dislocations rises sharply at the strain of 4%. It is noteworthy that before the strain is 4%, the density of other dislocations in the HEA is zero. After the strain of 6%, the density of total dislocations, the main dislocation 1/2<111> and other dislocations in the HEA tends to be stable, corresponding to the stable stress stage in the stress-strain curve. For the HEA-L, the density of total dislocations, the main dislocation 1/2<111> and other dislocations is basically unchanged. The dislocation density remains constant because the dynamic balance between dislocation creation from the grain boundaries between different layers and the annihilation at the sample free surface. The effect of sample size on the dislocation density was studied as it affects significantly the deformation behaviour. In

addition to the original specimen size of the HEA-L ($20 \times 5.0 \times 40$ nm^3), two other different sizes ($15 \times 5.0 \times 30$ nm^3 and $30 \times 5.0 \times 60$ nm^3) were also investigated. While keeping the same number of layers, the layer width is increased by increasing the sample size. It is found that the initial dislocation density of the undeformed HEA-L with the size in the x-direction being 15, 20 and 30 nm is 0.91×10^{17} /m^2, 1.35×10^{17} /m^2, and 1.67×10^{17} /m^2, respectively, which suggests the increase of dislocation density as the specimen size increases. This is because the large-sized HEA-L can trigger more grain boundary areas. The more grain boundaries (as weak regions) provide more nucleated positions and lower nucleated barriers to the dislocation, enhancing the dislocation density and structural heterogeneity. In general, the sample-size dependent crystal plasticity is an extensively studied topic [44]. However, the sample size effect in HEAs has yet to be fully addressed, and is very worthy for further investigation.

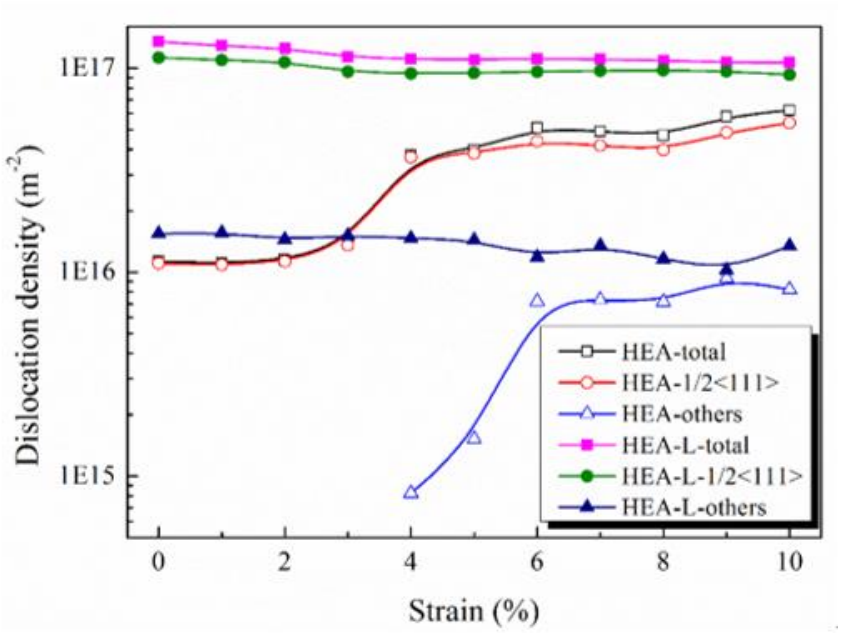

Fig. 8 The dislocation density–strain curves of the HEA and the HEA-L. The density of total dislocations, the main dislocation 1/2<111> and other dislocations are shown, respectively.

3.4. Microstructure

In order to quantify the atomic defects topology, the quasi-nearest atoms (QNAs) are calculated, as shown in Fig. 9, which is based on Voronoi analysis. If two atoms are a pair of QNAs, they should meet the following three conditions: (1) they share a common nearest neighbor; (2) their corresponding Voronoi faces of the Voronoi polyhedron centered by their common nearest neighbor share an edge; and (3) they are not the nearest neighbors of each other [45]. The number of QNAs (N_Q) can represent the degree of the atomic vacancies in BCC HEAs. The larger the N_Q around an atom, the more vacancies around the atom. N_Q = 0 or 1 means that the atomic vacancy of the central atom is zero or one, implying that the central atom subjected to many constraints is not easy to move. To reflect the deformation ability, only atoms with N_Q larger than 1 are shown in the HEA and the HEA-L prior to deformation. As shown in Fig. 9, the defects characterized by QNA are abundant in the grain boundaries of the HEA-L, increasing structural heterogeneity and providing nucleation sites for dislocations.

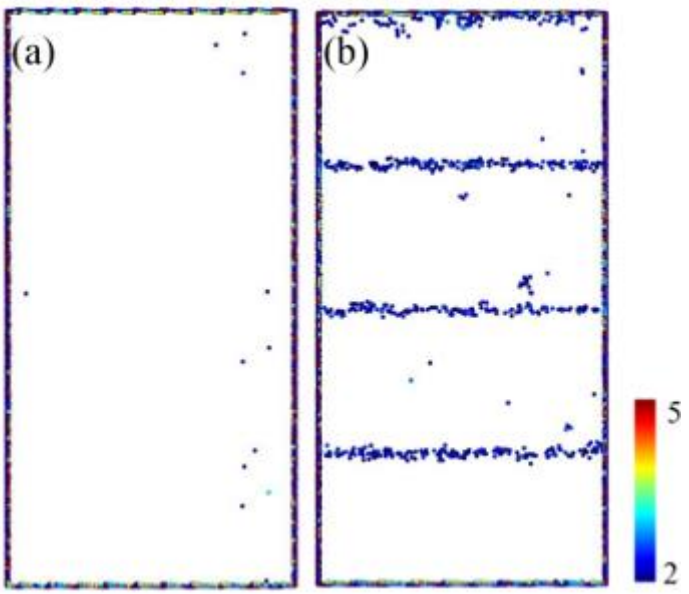

Fig. 9 Atoms with the number of QNA (N_Q) larger than 1 are shown in (a) the HEA and (b) the HEA-L prior to deformation.

Due to differences in the chemical bonding and atomic size, crystalline lattices of HEAs are severely distorted, making it difficult for atoms to move. For a more intuitive representation of the grain orientations in the HEA and the HEA-L, common neighbor analysis (CNA) is applied, which can satisfactorily distinguish different lattice types [46]. The selection of the cutoff radii between atoms is very critical, so the adaptive CNA with automatical variable cut-offs is applied [40]. The CNA parameters of the HEA and the HEA-L at 300 K are shown in Fig. 10a and Fig. 10b. The fraction of the BCC phase in the HEA is 94.8%, while that in the HEA-L is 87%, speaking to the fact that the cooling rate gradient increases the structural disorder in the HEA-L. The atomic potential energy characterizing the atomic mobility in the initial structure of the HEA and the HEA-L are also calculated. Only atoms with potential energy greater than -4 eV/atom are shown for better comparison. Compared to the distorted lattices, there are many atoms with large potential energy in the HEA-L, as shown in Fig. 10d. Due to atomic disorder and high potential energy, atoms at the grain boundaries are more likely to move, and the barriers of dislocations are lower than those in distorted lattices [47].

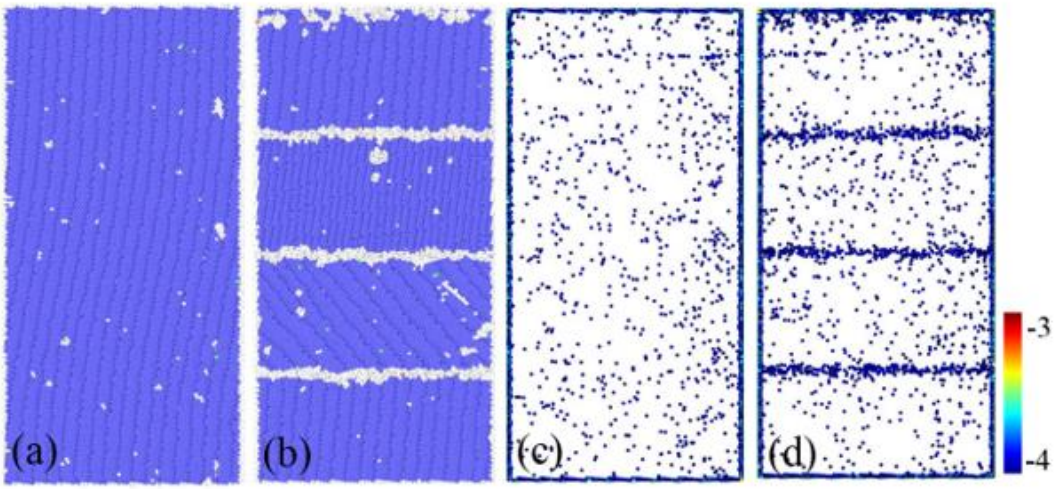

Fig. 10 The CNA parameters of (a) the HEA and (b) the HEA-L. Color denotes atomic structure: blue, BCC and white, others. Atoms with potential energy larger than -4 eV/atom are displayed in (c) the HEA and (d) the HEA-L.

The fraction of partial coordination number for Cu, Co, Ni, Cr and Al atoms in grain interiors and grain boundaries of the $Cu_{0.5}CoNiCrAl$ HEA-L is shown in Fig. 11. In grain interiors, the distribution of partial coordination number for Cu, Co, Ni, Cr and Al atoms is homogeneous, while that in grain boundaries is obviously heterogeneous. This suggests that chemical segregation occurs at the grain boundaries, which could facilitate formation of dislocations. Detailed study on the segregation effect are taking places, and will be reported in the future publication. Therefore, the grain boundaries formed via the cooling rate gradient, as weak regions, provide more nucleation sites with lower nucleation barriers for the dislocations, improving structural heterogeneity. As the strain increases, these weak regions gradually stimulate the distorted lattice to participate in the deformation, triggering the formation of multiple dislocations and enhancing the deformation ability of the HEA-L. The effect of grain boundary on enhancing deformability of BCC HEAs has also been observed experimentally [48].

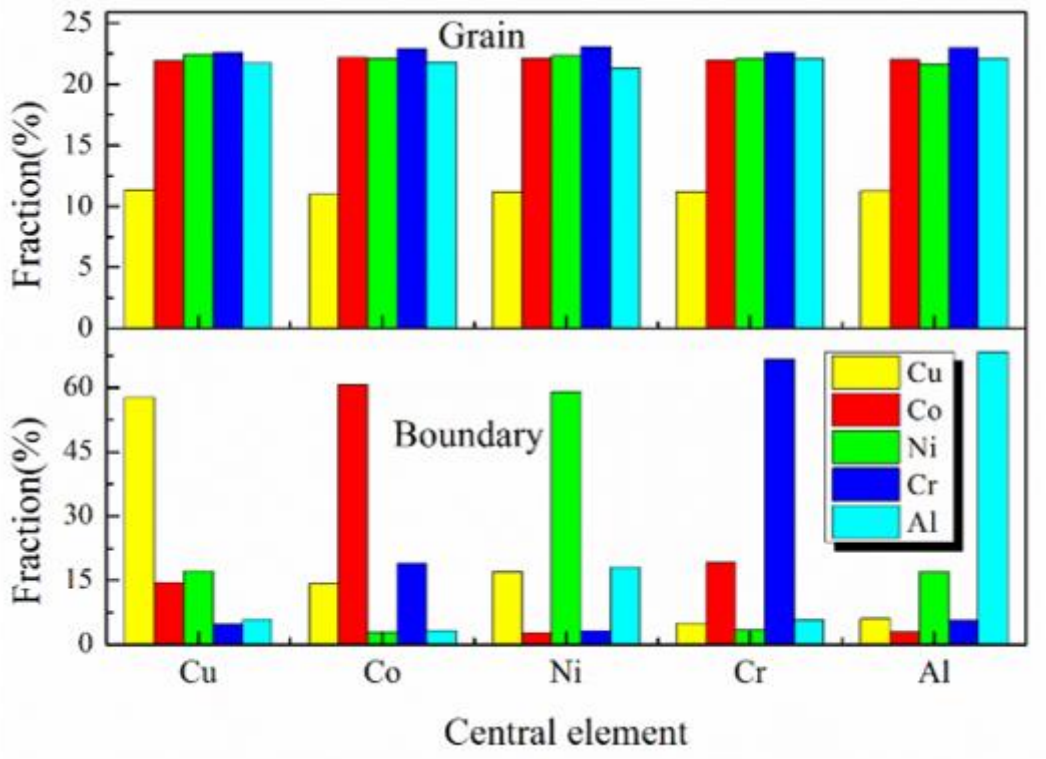

Fig. 11 The fraction of partial coordination number for Cu, Co, Ni, Cr and Al atoms in grain interiors and grain boundaries of the $Cu_{0.5}CoNiCrAl$ HEA-L.

3.5. Schematic description

The cooling rate gradient can promote different grain orientations in HEAs, leading to the formation of the HEA-L. When compared to the HEA, the HEA-L shows the enhancement of stable deformation ability. The mechanistic understanding of the effect of cooling rate gradient on the HEA-L is postulated in Fig. 12. In the single-crystalline $Cu_{0.5}$CoNiCrAl BCC HEA, a highly localized slip band is developed at the strain of 4%. Correspondingly, the 45° dislocation lines with Burges vector 1/2<111> are formed throughout the BCC HEA at the strain of 4%. Zou et al. found that the nanoscale single-crystalline BCC HEA pillar can fail via slip bands oriented at ~40-70° off the loading axis, which is attributed to the cross-slip of screw dislocations along <111> directions [49], verifying the reliability of our model. In general, the BCC metals have larger lattice resistance (i.e., Peierls stress) than that of FCC metals, rendering that the activation of multiple shear paths could be more difficult. In addition to the Peierls barrier, the lattice distortion effect of HEAs is more prominent in the BCC phase. For example, Wang and Zou et al. found that higher lattice distortion can lead to greater lattice resistance, amplifying the effective Peierls barrier in BCC HEAs [49, 50]. The above suggests that the obtained results (localized slip bands and 45° dislocation lines with Burges vector 1/2<111>) are originated from the BCC structure. In the HEA-L, multiple strain paths associated different slip systems are triggered. As the strain increases, these strain paths gradually intersect and overlap, propagating in multiple directions to avoid the formation of localized deformation. This enhanced deformability is attributed to multiple dislocations of the HEA-L, which are closely related to the atomic features in the HEA-L structure. The introduction of cooling rate gradient increases defects, disorder and atomic potential energy of the HEA-L, providing more nucleated positions and lower nucleated barriers to the dislocations.

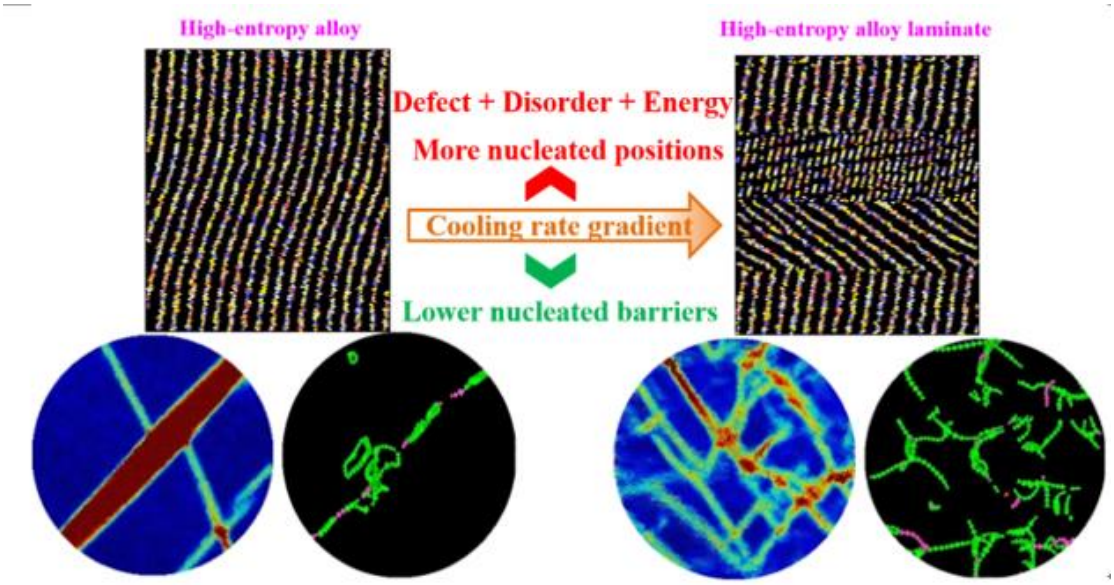

Fig. 12 Schematic description of the effect of cooling rate gradient on the HEA-L.

4. Conclusions

The $Cu_{0.5}CoNiCrAl$ HEAs processed by the cooling rate gradient were investigated by MD simulations. The cooling rate gradient can significantly enhance the deformation ability of HEAs by promoting different grain orientations, avoiding a highly localized strain path. The defects characterized by QNA are abundant in the grain boundaries, providing nucleation sites of the dislocations in HEA-L. The introduction of structural disorder, high potential energy and chemical segregation via the cooling rate gradient lowers the nucleation barriers of dislocations. The grain boundaries formed via the cooling rate gradient, as weak regions, provide more nucleated positions and lower nucleated barriers to the dislocation, improving structural heterogeneity and promoting the formation of multiple dislocations. These results provide a guide to the design of plastically enhanced HEAs.

Acknowledgments

This work was supported by the National Natural Science Foundation of China under Grant 51801174; and the Program for the Top Young Talents of Higher Learning

Institutions of Hebei under Grant BJ2018021; the Hong Kong Scholars Program under Grant XJ2017049; and the Hong Kong Polytechnic University under Grant G-YZ1J. LL acknowledges the support from the US National Science Foundation under Grant CMMI 17-0267.

Additional Information

Declarations of interest: none.

References

[1] J.W. Yeh, S.K. Chen, S.J. Lin, J.Y. Gan, T.S. Chin, T.T. Shun, C.H. Tsau, S.Y. Chang, Nanostructured high-entropy alloys with multiple principal elements: novel alloy design concepts and outcomes, Adv. Eng. Mater. 6(5) (2004) 299-303.

[2] Z.F. Lei, X.J. Liu, Y. Wu, H. Wang, S.H. Jiang, S. Wang, X.D. Hui, Y.D. Wu, B. Gault, P. Kontis, D. Raabe, L. Gu, Q.H. Zhang, H.W. Chen, H.T. Wang, J.B. Liu, K. An, Q.S. Zeng, T.G. Nieh, Z.P. Lu, Enhanced strength and ductility in a high-entropy alloy via ordered oxygen complexes, Nature 563(7732) (2018) 546-550.

[3] Y.X. Ye, B.L. Musico, Z.Z. Lu, L.B. Xu, Z.F. Lei, V. Keppens, H.X. Xu, T.G. Nieh, Evaluating elastic properties of a body-centered cubic NbHfZrTi high-entropy alloy – A direct comparison between experiments and ab initio calculations, Intermetallics 109 (2019) 167-173.

[4] Y. Zhang, T.T. Zuo, Z. Tang, M.C. Gao, K.A. Dahmen, P.K. Liaw, Z.P. Lu, Microstructures and properties of high-entropy alloys, Prog. Mater. Sci. 61 (2014) 1-93.

[5] W. Li, P. Liu, P.K. Liaw, Microstructures and properties of high-entropy alloy films and coatings: a review, Mater. Res. Lett. 6(4) (2018) 199-229.

[6] A. Sharma, S.A. Deshmukh, P.K. Liaw, G. Balasubramanian, Crystallization kinetics in AlxCrCoFeNi ($0 \leq x \leq 40$) high-entropy alloys, Scripta Mater. 141 (2017) 54-57.

[7] K. Zhang, S. Pan, W. Tang, Y. Zhang, B. Wei, Structural and bonding transformation of $Al_{0.67}$CrCoCuFeNi high-entropy alloys during quenching, J. Alloys Compd. 753 (2018) 636-641.

[8] D.B. Miracle, O.N. Senkov, A critical review of high entropy alloys and related concepts, Acta Mater. 122 (2017) 448-511.

[9] E.W. Huang, D. Yu, J.W. Yeh, C. Lee, K. An, S.Y. Tu, A study of lattice elasticity from low entropy metals to medium and high entropy alloys, Scripta Mater. 101 (2015) 32-35.

[10] Z. Wu, H. Bei, G.M. Pharr, E.P. George, Temperature dependence of the mechanical properties of equiatomic solid solution alloys with face-centered cubic crystal structures, Acta Mater. 81 (2014) 428-441.

[11] S.F. Liu, Y. Wu, H.T. Wang, J.Y. He, J.B. Liu, C.X. Chen, X.J. Liu, H. Wang, Z.P. Lu, Stacking fault energy of face-centered-cubic high entropy alloys, Intermetallics 93 (2018) 269-273.

[12] T. Zuo, M. Zhang, P.K. Liaw, Y. Zhang, Novel high entropy alloys of FexCo1-xNiMnGa with excellent soft magnetic properties, Intermetallics 100 (2018) 1-8.

[13] S.Y. Huang, Y.F. Gao, K. An, L.L. Zheng, W. Wu, Z.K. Teng, P.K. Liaw, Deformation mechanisms in a precipitation-strengthened ferritic superalloy revealed by in situ neutron diffraction studies at elevated temperatures, Acta Mater. 83 (2015) 137-148.

[14] M.J. Yao, K.G. Pradeep, C.C. Tasan, D. Raabe, A novel, single phase, non-equiatomic FeMnNiCoCr high-entropy alloy with exceptional phase stability and tensile ductility, Scripta Mater. 72-73 (2014) 5-8.

[15] J.Y. He, W.H. Liu, H. Wang, Y. Wu, X.J. Liu, T.G. Nieh, Z.P. Lu, Effects of Al addition on structural evolution and tensile properties of the FeCoNiCrMn high-entropy alloy system, Acta Mater. 62 (2014) 105-113.

[16] W. Li, P.K. Liaw, Y. Gao, Fracture resistance of high entropy alloys: A review, Intermetallics 99 (2018) 69-83.

[17] B. Gludovatz, A. Hohenwarter, D. Catoor, E.H. Chang, E.P. George, R.O. Ritchie, A fracture-resistant high-entropy alloy for cryogenic applications, Science 345(6201) (2014) 1153-8.

[18] B. Wang, H. He, M. Naeem, S. Lan, S. Harjo, T. Kawasaki, Y. Nie, H.W. Kui, T. Ungár, D. Ma, A.D. Stoica, Q. Li, Y. Ke, C.T. Liu, X.L. Wang, Deformation of CoCrFeNi high entropy alloy at large strain, Scripta Mater. 155 (2018) 54-57.

[19] J.Y. He, H. Wang, H.L. Huang, X.D. Xu, M.W. Chen, Y. Wu, X.J. Liu, T.G. Nieh, K. An, Z.P. Lu, A precipitation-hardened high-entropy alloy with outstanding tensile properties, Acta Mater. 102 (2016) 187-196.

[20] J. Ding, Q. Yu, M. Asta, R.O. Richie, Tunable stacking fault energies by tailoring local chemical order in CrCoNi medium-entropy alloys, Proc. Natl. Acad. Sci. USA 115 (2018) 8919-8924.

[21] S. Fu, H. Bei, Y. Chen, T.K. Liu, D. Yu, K. An, Deformation mechanisms and work-hardening behavior of transformation-induced plasticity high entropy alloys by *in-situ* neutron diffraction, Mater. Res. Lett. 6(11) (2018) 620-626.

[22] S.G. Ma, S.F. Zhang, J.W. Qiao, Z.H. Wang, M.C. Gao, Z.M. Jiao, H.J. Yang, Y. Zhang, Superior high tensile elongation of a single-crystal $CoCrFeNiAl_{0.3}$ high-entropy alloy by Bridgman solidification, Intermetallics 54 (2014) 104-109.

[23] H. Huang, Y. Wu, J. He, H. Wang, X. Liu, K. An, W. Wu, Z. Lu, Phase-transformation ductilization of brittle high-entropy alloys via metastability engineering, Adv. Mater. 29(30) (2017).

[24] X.W. Zhou, R.A. Johnson, H.N.G. Wadley, Misfit-energy-increasing dislocations in vapor-deposited CoFe/NiFe multilayers, Phys. Rev. B 69(14) (2004) 144113.

[25] H.N.G. Wadley, X.W. Zhou, R.A. Johnson, M. Neurock, Mechanisms, models and methods of vapor deposition, Prog. Mater. Sci. 46(3-4) (2001) 329-377.

[26] X.W. Zhou, H.N.G. Wadley, R.A. Johnson, D.J. Larson, N. Tabat, A. Cerezo, A. Petford Long, G.D.W. Smith, P.H. Clifton, R.L. Martens, Atomic scale structure of sputtered metal multilayers, Acta Mater. 49(19) (2001) 4005-4015.

[27] X.W. Zhou, H.N.G. Wadley, Atomistic simulation of the vapor deposition of Ni/Cu/Ni multilayers: Incident adatom angle effects, J. Appl. Phys. 87(1) (2000) 553-563.

[28] X.W. Zhou, H.N.G. Wadley, Atomistic simulations of the vapor deposition of Ni/Cu/Ni multilayers: The effects of adatom incident energy, J. Appl. Phys. 84(4) (1998) 2301-2315.

[29] L. Xie, P. Brault, A.L. Thomann, J.M. Bauchire, AlCoCrCuFeNi high entropy alloy cluster growth and annealing on silicon: A classical molecular dynamics simulation study, Appl. Surf. Sci. 285 (2013) 810-816.

[30] L. Xie, P. Brault, A.L. Thomann, X. Yang, Y. Zhang, G. Shang, Molecular dynamics simulation of Al–Co–Cr–Cu–Fe–Ni high entropy alloy thin film growth, Intermetallics 68 (2016) 78-86.

[31] S.I. Rao, C. Varvenne, C. Woodward, T.A. Parthasarathy, D. Miracle, O.N. Senkov, W.A. Curtin, Atomistic simulations of dislocations in a model BCC

multicomponent concentrated solid solution alloy, Acta Mater. 125 (2017) 311-320.

[32] J.W. Yeh, S.J. Lin, T.S. Chin, J.Y. Gan, S.K. Chen, T.T. Shun, C.H. Tsau, S.Y. Chou, Formation of simple crystal structures in Cu-Co-Ni-Cr-Al-Fe-Ti-V alloys with multiprincipal metallic elements, Metall. Mater. Trans. A 35(8) (2004) 2533-2536.

[33] M.C. Gao, J.-W. Yeh, P.K. Liaw, Y. Zhang, High-entropy alloys, Cham: Springer International Publishing (2016).

[34] C.Y. Yu, X.D. Xu, M.W. Chen, C.T. Liu, Atomistic mechanism of nano-scale phase separation in fcc-based high entropy alloys, J. Alloys Compd. 663 (2016) 340-344.

[35] A. Sharma, P. Singh, D.D. Johnson, P.K. Liaw, G. Balasubramanian, Atomistic clustering-ordering and high-strain deformation of an $Al_{0.1}$CrCoFeNi high-entropy alloy, Sci. Rep. 6 (2016) 31028.

[36] S. Plimpton, Fast parallel algorithms for short-range molecular dynamics, J. Comput. Phys. 117(1) (1995) 1-19.

[37] S. Nose, A unified formulation of the constant temperature molecular dynamics methods, J. Chem. Phys. 81(1) (1984) 511-519.

[38] M. Parrinello, A. Rahman, Polymorphic transitions in single crystals: A new molecular dynamics method, J. Appl. Phys. 52(12) (1981) 7182-7190.

[39] A.J. Cao, Y.Q. Cheng, E. Ma, Structural processes that initiate shear localization in metallic glass, Acta Mater. 57(17) (2009) 5146-5155.

[40] A. Stukowski, Visualization and analysis of atomistic simulation data with OVITO–the Open Visualization Tool, Modell. Simul. Mater. Sci. Eng. 18(1) (2010) 015012.

[41] P.M. Larsen, S. Schmidt, J. Schiøtz, Robust structural identification via polyhedral template matching, Modell. Simul. Mater. Sci. Eng. 24(5) (2016) 055007.

[42] F. Shimizu, S. Ogata, J. Li, Theory of shear banding in metallic glasses and molecular dynamics calculations, Mater. Trans. 48(11) (2007) 2923-2927.

[43] A. Stukowski, V.V. Bulatov, A. Arsenlis, Automated identification and indexing of dislocations in crystal interfaces, Modell. Simul. Mater. Sci. Eng. 20(8) (2012) 085007.

[44] J.R. Greer, J.T.M. De Hosson, Plasticity in small-sized metallic systems: Intrinsic versus extrinsic size effect, Prog. Mater. Sci. 56(6) (2011) 654-724.

[45] S.P. Pan, S.D. Feng, L.M. Wang, J.W. Qiao, X.F. Niu, B.S. Dong, W.M. Wang, J.Y. Qin, Structural disorder in metallic glass-forming liquids, Sci. Rep. 6 (2016) 27708.

[46] D. Faken, H. Jónsson, Systematic analysis of local atomic structure combined with 3D computer graphics, Comput. Mater. Sci. 2(2) (1994) 279-286.

[47] D. Bacon, Y. Osetsky, D. Rodney, Dislocation–obstacle interactions at the atomic level, Dislocations in solids 15 (2009) 1-90.

[48] Y. Zou, H. Ma, R. Spolenak, Ultrastrong ductile and stable high-entropy alloys at small scales, Nat. Commun. 6 (2015) 7748.

[49] Y. Zou, S. Maiti, W. Steurer, R. Spolenak, Size-dependent plasticity in an $Nb_{25}Mo_{25}Ta_{25}W_{25}$ refractory high-entropy alloy, Acta Mater. 65 (2014) 85-97.

[50] S. Wang, Atomic structure modeling of multi-principal-element alloys by the principle of maximum entropy, Entropy 15(12) (2013) 5536-5548.